Nanoscale Intermittent Contact-Scanning Electrochemical Microscopy

Robert A. Lazenby,[1] Kim McKelvey,[1,2] Massimo Peruffo,[1] Marc Baghdadi[1,2] and Patrick R. Unwin[*,1]*

[1] Department of Chemistry, University of Warwick, Coventry, U.K., CV4 7AL.

[2] Molecular Organization and Assembly in Cells (MOAC) Doctoral Training Centre (DTC), University of Warwick, Coventry, U.K. CV4 7AL.

*Corresponding author: e-mail P.R.Unwin@warwick.ac.uk, telephone +44 (0) 2476 523264, fax : +44 (0) 2476 524112.

Submitted to J. Solid State Electrochem., Bard Festschrift, April 2013

Contribution to the Festschrift for Allen J. Bard, on the occasion of his 80th birthday.

Abstract

A major theme in scanning electrochemical microscopy (SECM) is methodology for nanoscale imaging with distance control and positional feedback of the tip. We report the expansion of intermittent contact (IC)-SECM to the nanoscale, using disk-type Pt nanoelectrodes prepared using the laser-puller sealing method. The Pt was exposed using a focused ion beam milling procedure to cut the end of the electrode to a well-defined glass sheath radius, which could also be used to reshape the tips to reduce the size of the glass sheath. This produced nanoelectrodes that were slightly recessed, which was optimal for IC-SECM on the nanoscale, as it served to protect the active part of the tip. A combination of finite element method simulations, steady-state voltammety and scanning electron microscopy, for the measurement of critical dimensions, was used to estimate Pt recession depth. With this knowledge, the tip-substrate alignment could be further estimated by tip approach curve measurements. IC-SECM has been implemented by using a piezo-bender actuator for the detection of damping of the oscillation amplitude of the tip, when IC occurs, which was used as a tip position feedback mechanism. The piezo-bender actuator improves significantly on the performance of our previous setup for IC-SECM, as the force acting on the sample due to the tip is greatly reduced, allowing studies with more delicate tips. The capability of IC-SECM is illustrated with studies of a model electrode (metal/glass) substrate.

Keywords: SECM; nanoelectrode; nanoscale electrochemical imaging; focused ion beam (FIB) milling.

Introduction

Since its inception, about two decades ago by Bard and co-workers [1], imaging using scanning electrochemical microscopy (SECM) has mainly been limited to the use of ultramicroelectrode (UME) tips with characteristic dimensions on the 1-25 μm scale [2, 3]. For nanoscale electrochemical imaging, *i.e.* the use of electrodes of several hundred nanometers active diameter or smaller, which operate at (similar or smaller) nanoscale distances from the substrate, a positional feedback mechanism is necessary, unless imaging is over small areas on a flat substrate and with stringent isothermal conditions [4]. SECM imaging without positional feedback, known as constant-height mode, leaves the tip susceptible to crashing into or drifting away from the surface, especially if the tip and substrate are not well aligned, or there is creep in the piezoelectric positioners.

Various attempts have been made to implement independent tip-substrate distance control and measurement for SECM at the nanoscale. Shear-force distance regulation has been used to provide positional feedback [5, 6], with constant-distance nanoscale imaging achieved [7]. The tip resonates laterally and the amplitude of this oscillation decreases when the tip is moved within a few hundred nanometers of the surface, due to the shear forces acting between tip and substrate [8-10]. Wipf and Bard introduced tip-position modulation (TPM) SECM [11], in which the tip is oscillated with a small amplitude in the direction perpendicular to the substrate and the resulting AC and DC currents are measured. In principle, this can be used to determine both the activity and topography of a surface [12] and this approach can also be used for distance control [13].

A constant-distance mode, in which the tip traces the contours of the surface based on the tip current, has been used [14], but there is the issue of how to separate unambiguously the topography and activity of the sample; a problem which can be addressed by implementing a voltage switching mode [15]. Another approach has been to integrate an UME into a tip for atomic force microscopy (AFM), in combined SECM-AFM [16-20], with high resolution tips having been made using nanowires grown on single-walled carbon nanotubes [21]. Nanoscale SECM is also possible by performing the scan in a thin liquid layer, which means the tip does not require insulation, in a technique comparable to scanning tunneling microscopy (STM) [22]. An ion current between two ideally non-polarizable electrodes can also be used to provide pure distance control, as demonstrated by scanning ion conductance microscopy (SICM) [23]. Tips having two electrodes have been successfully used for dual function imaging: a SICM component for topography, and a solid electrode for redox activity imaging [24-26].

An issue of many combined techniques is that they often require the fabrication of specially-designed tips. However, positional feedback can also be achieved with conventional SECM probes. This has most recently been seen in intermittent contact (IC)-SECM [27], where the tip is oscillated normal to the surface of interest (as in TPM) and upon physical contact between tip and substrate the oscillation is damped, which can be used as a setpoint for approach curve measurements and imaging. This technique has already been implemented for the visualization of electrode activity [28], for non-

electrochemical tip positioning [29] and for probing molecular transport across dentin [30]. However, in all of these applications, IC-SECM has so far been limited to micron-scale probes.

The preparation of Pt disk nanoelectrodes is now well known [31-33], with electrode radii as low as 1 nm reported [34]. Nanoelectrodes have recently been reviewed [35], and reports of such tips being used for nanoscale electrochemical imaging in SECM are now appearing [36, 37]. Polished Pt-disk nanoelectrodes have been used for constant-height imaging, using an electrochemical response to determine topography [36], and similar probes have also been used for electrochemical imaging of cells [37]. For pulled Pt tips, the Pt may be exposed using hydrofluoric acid to etch the glass to produce a finite cone-shaped electrode [38], or by micropolishing the tip to produce a disk electrode [32]. Here, we use a robust and reliable method to focused ion beam (FIB) mill tips to ensure a flat electrode, with a recessed Pt disk, that is cut to a precise glass sheath thickness to give a probe with a typical RG value, defined as the ratio of the radius of the insulating glass sheath, r_{glass}, to the radius of the electrode, a. The FIB milling procedure has been used in the production of SECM-SICM tips [24, 26]. Here it is used to shape electrodes to yield symmetrical probes with RG values close to 10. Although we used FIB milling for tip fabrication here, electrode micropolishing is a more readily available alternative, but control over tip geometry and size would be more challenging.

In order to implement nanoscale IC-SECM, we also report improvements on the original instrument design [27], with the introduction of a piezo-bender actuator, which has a much smaller spring constant than the piezoelectric positioner used previously [27], and provides greater sensitivity in the detection of tip oscillation amplitude damping. This is a key requirement for the implementation of IC-SECM with fragile nanoelectrodes.

Experimental Section

Materials. S*olutions.* Ferrocenylmethyltrimethylammonium ($FcTMA^+$) hexafluorophosphate, prepared from the metathesis of the iodide salt (Strem Chemicals) and silver hexafluorophosphate (Strem Chemicals), was used at a concentration of 1 mM in 0.1 M potassium chloride (Aldrich, ACS Reagent grade) solution, made up using water purified (deionised) through a Millipore Milli-Q system (resistivity 18.2 MΩ cm at 25 °C).

Substrate. A gold band, of height 125 nm determined by AFM, on a glass microscope slide was used as a model substrate. The AFM image was recorded in tapping mode using a Veeco Enviroscope with Nanoscope IV controller. The AFM image was processed using the SPIPsoftware package (Image Metrology).

Electrode fabrication. Nanoelectrode tips, comprising of Pt sealed in glass, were prepared following a closely similar procedure to that described by Zuliani *et al.* [33] which is based on an earlier report [32], for quartz capillaries (0.50 mm inner diameter; 1.00 mm outer diameter; 10 cm length), using a Sutter P-2000 laser puller with modification of the settings (Program 1: HEAT = 830 ± 20; FILAMENT = 5; VELOCITY = 255; DELAY = 255; PULL = 0. Program 2: HEAT = 690;

FILAMENT = 1; VELOCITY = 43; DELAY = 124; PULL = 120). The Pt was exposed by removing the ends of the nanotips by FIB milling, using a FIB scanning electron microscope (SEM) (JEOL 4500, JEOL), at an accelerating voltage of 5 kV, with positively charged Ga^+ ions at 5 nC μm^{-2}. Low resolution images were obtained using the JEOL system to follow the FIB milling procedure, but higher resolution field emission (FE) SEM micrographs of the tips, for the measurement of critical dimensions, were acquired at 15 kV, using a SUPRA 55 variable-pressure system (Zeiss). FIB-milled tips with exposed Pt were also shaped, to reduce the RG value to around 10, and to ensure that the Pt was located centrally in the glass sheath of the probe. This was done by defining a mask over the end of the tip, and milling the region inside this, in the same manner as for cutting the tips.

Instrumentation. The instrument used for the studies herein was modified from our previous design for IC-SECM [27], specifically in order to implement low-force soft-tapping imaging with nanoelectrodes. Coarse control of the SECM tip, mounted perpendicular to the surface, was realized using a motorized *x*, *y*, *z* translation stage (M-112.1DG, Physik Instrumente) controlled by a motion controller card (C843.41, Physik Instrumente). Fine control was realized by three piezoelectric positioners for closed loop operation: two (*x* and *y*) each with 500 μm total travel (PIHera P-625.2CD, Physik Instrumente), controlled through a digital piezo controller (E761, Physik Instrumente), and one positioner (*z*) with 100 μm travel (PIHera P-621.ZCD, Physik Instrumente) for operation with an amplifier/servo (E.665 LVPZT, Physik Instrumente). The piezoelectric positioner amplifier/servo and digital piezo controller were controlled through a data acquisition (DAQ) card (NI PCIe-6259, National Instruments) from a PC running custom LabVIEW code (LabVIEW 9.0, National Instruments).

The SECM tip was held in place on a tip holder mounted directly onto a piezo-bender actuator fitted with a strain gauge sensor (SGS) (PICMA P-871.112, Physik Instrumente), operated with an amplifier/servo (E-651.1S, Physik Instrumente), mounted onto the *z*-piezoelectric positioner. A sinusoidal oscillation was generated using a sine wave generator (Digimess TG100, Digimess) and applied to the piezo-bender actuator. A schematic of the modified setup is given in Fig. 1.

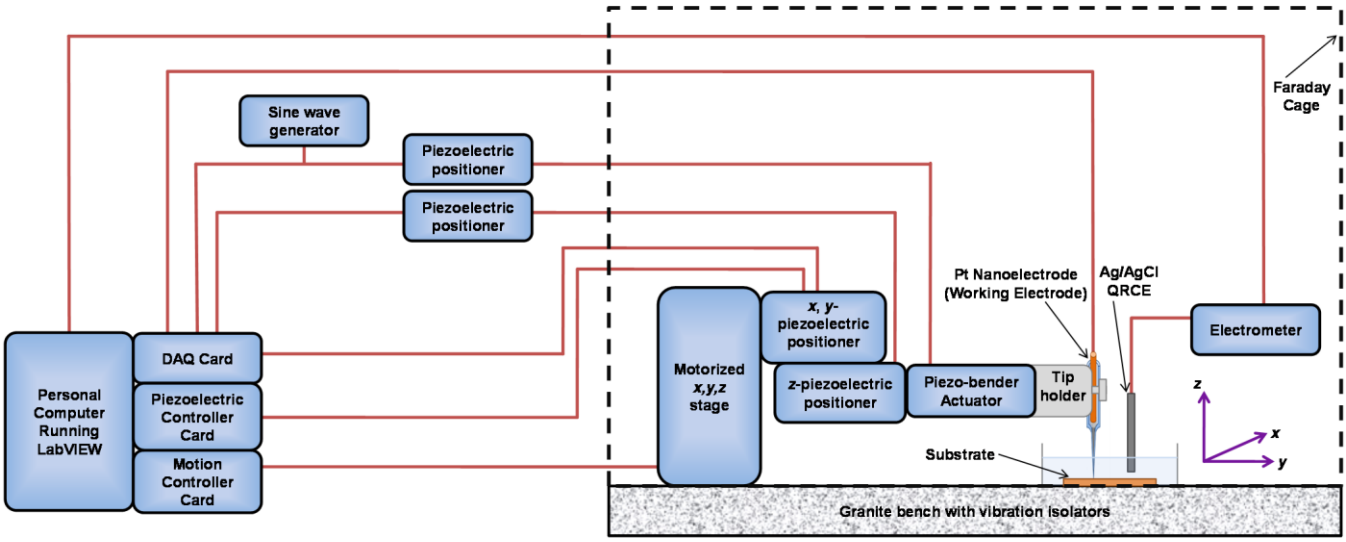

Fig. 1 Schematic showing the setup of IC-SECM with a piezo-bender actuator

An AgCl-coated Ag wire (Ag/AgCl) served as a quasi-reference counter electrode (QRCE) in a two-electrode configuration. The SECM was operated in the feedback mode, by applying a potential of 0.45 V to the Pt nanoelectrode *vs*. the Ag/AgCl QRCE, whilst the substrate was unbiased. This potential corresponded to the diffusion-limited one-electron oxidation of $FcTMA^+$ to $FcTMA^{2+}$ at the tip.

IC-SECM approach curves and imaging. While oscillated with a small amplitude in *z*, the tip was approached normal to the surface of interest (*z*-direction) using the *z*-piezoelectric positioner. Detection of IC for the tip approach and the imaging process have been described previously in full [27], but was slightly different here because the piezo-bender actuator was oscillated and used to detect damping rather than the *z*-piezoelectric positioner. In brief, the tip was oscillated at 70 Hz with an amplitude of about 36 nm, and a damping of 5 % in the oscillation amplitude was used as the setpoint for imaging. The scan area was typically 3 μm × 3 μm, with a 0.1 μm step size in each direction. A forward line scan was made in intermittent contact, and a reverse line scan was made at a constant distance of 300 nm from the forward scan *z*-position, using the tip-contact data detected on the forward line scan to set the tip position in *z* on the reverse scan.

Simulations

Recessed electrodes. Steady-state finite element method (FEM) simulations of mass transport to a recessed disk-shaped UME were carried out to quantify the effect of electrode recession on the diffusion-limited current in a 1 mM $FcTMA^+$ solution. A steady-state diffusion equation (Fick's second law), describes the mass transport of $FcTMA^+$ in this system,

$$D\nabla^2 c = 0, \tag{1}$$

where D is the diffusion coefficient, which is set to 6.0×10^{-6} cm^2 s^{-1} [39], and c is the concentration of $FcTMA^+$. Rotational symmetry allowed a two dimensional (2D) axisymmetric cylindrical geometry to be used, as shown in Fig. 2. The electrode radius, a in Fig. 2, was set to 70 nm and the amount of glass surround was set to 10a. These critical tip dimensions were based on SEM measurements of the electrode used, which was done for each electrode studied. The size of the simulation, b in Fig. 2, was set to 50 μm, and the recession depth, r in Fig. 2, varied. The concentration of $FcTMA^+$ at the electrode (boundary 2 in Fig. 2) was set to zero (c = 0). The glass area of the electrode (boundaries 3, 4 and 5 in Fig. 2) were set to no flux ($\nabla c \cdot n = 0$), where n is the unit normal vector. The bulk solution (boundaries 6, 7 and 8 in Fig. 2) was set to bulk concentration (c = 1 mM). Finally, the rotational symmetry axis (boundary 1 in Fig. 2) was set as a symmetry boundary condition ($\nabla c \cdot n = 0$). Simulations were run on a personal computer (WindowsXP Pro 64 bit) using COMSOL Multiphysics 4.2 (Comsol AB, Sweden).

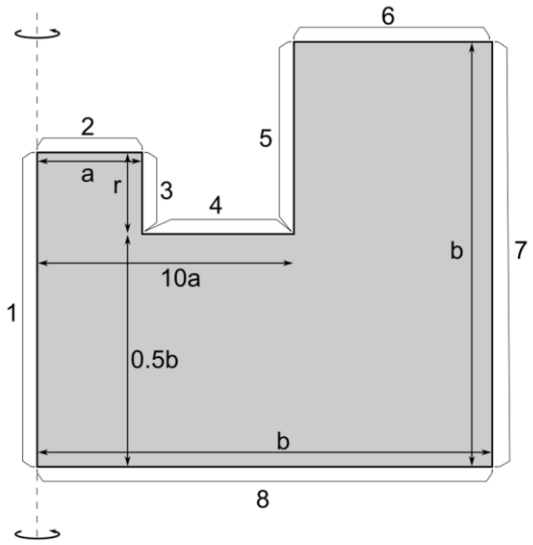

Fig. 2 The simulation domain (including dimensions and boundary labels), as described in the supporting text, for a 2D FEM simulation of a recessed planar disk-shaped UME. Not to scale

Approach curves. Steady-state FEM simulations of a recessed disk-shaped planar UME, at an angle with respect to an inert insulating substrate, and as a function of distance from the substrate, were carried out to quantify the effect of probe angle on the distance-dependent current (approach curve) response. As above, *equation (1)* (Fick's second law), describes the mass transport of $FcTMA^+$ to the electrode, but the incorporation of the probe angle breaks the rotational symmetry and therefore a three dimensional (3D) simulation, with one plane of mirror symmetry, was used. Fig. 3 shows a 2D diagram of the geometry, with probe dimensions, as well as the 3D simulation domain (which, again, is not drawn to scale), with the boundaries marked.

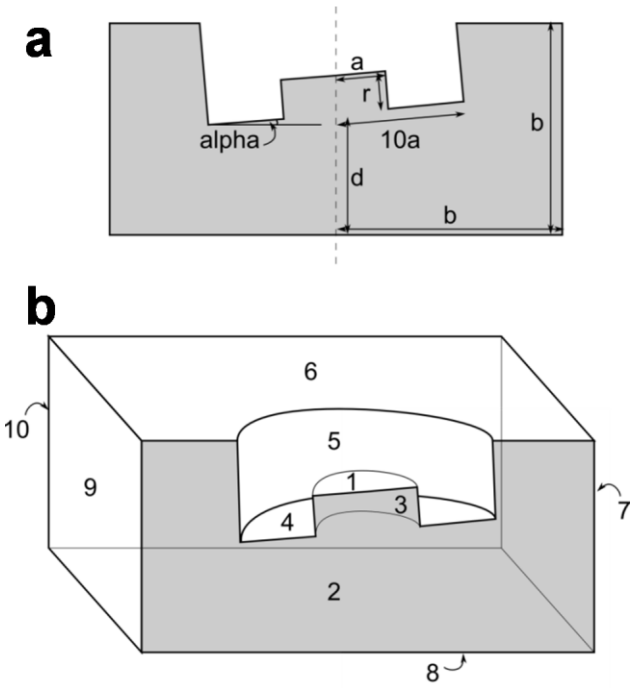

Fig. 3 (a) 2D representation of the geometry, including dimensions, of the angled recessed UME above a surface. (b) The simulation domain (including boundary labels), as described in the main text, for 3D FEM simulations of a recessed planar disk-shaped UME above an insulating surface. Not to scale

The simulation domain is defined by the probe dimensions, shown in Fig. 3a, and described above. In addition, the probe angle, alpha in Fig. 3a, and distance to the surface, *d* in Fig. 3a, are independent variables. The boundary conditions, shown in Fig. 3b, of the FEM simulation are as follows: 1 is the electrode surface and the concentration is set to zero ($c = 0$); 2 is the mirror symmetry plane and is set to have no normal flux ($\nabla c \cdot n = 0$); 3, 4 and 5 are the glass surrounds of the probe and are set to have no normal flux ($\nabla c \cdot n = 0$); 6, 7, 9 and 10 are the bulk solution and set to the bulk concentration ($c = 1$ mM); and 8 is the insulating surface and set to have no flux ($\nabla c \cdot n = 0$).

Results and Discussion

Tip characterization. Pt-disk nanoelectrodes were fabricated reproducibly and reliably with the active electrode radius typically in the range of 50 – 150 nm, exposed by FIB milling using the protocol shown schematically in Fig. 4a, in which a series of cuts are used to produce an electrode with a well-defined (and relatively small) RG value. As formed, nanoelectrodes were typically asymmetric, with an RG value between 20 and 30, and this is likely due to the position of the Pt wire in the glass capillary during the sealing step. A typical nanoelectrode is shown end-on in the SEM micrograph in Fig. 4b. This asymmetry has recently been studied, and for RG values in this range does not have any significant effect on the approach curve with respect to the value expected based on the average RG value [40]. As an extension to the FIB milling

procedure, Fig. 4c shows an electrode that has been 'shaped' in the milling process to produce a tip of preferred geometry, *i.e.* smaller RG and more central location of the Pt.

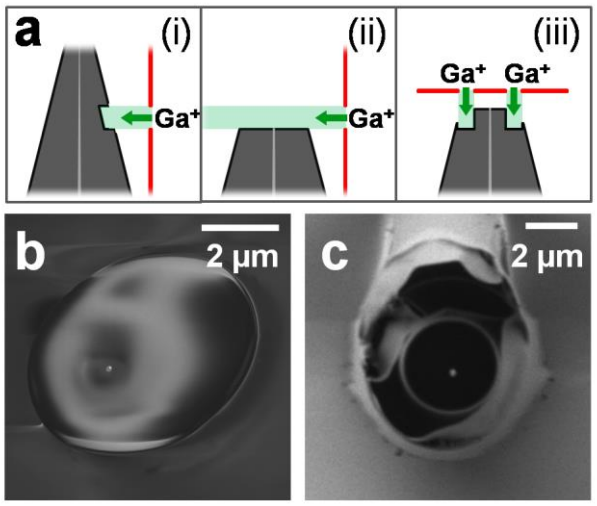

Fig. 4 Side-view schematic of the FIB-milling procedure (a) showing ablation during the milling (i), a cut nanoelectrode (ii) and reducing the RG of the cut electrode (iii). Top down view SEM micrographs of a Pt-disk nanoelectrode after FIB milling: (b) of the cut surface after the procedure in (aii) and (c) an electrode shaped by FIB milling

The dimension of the exposed Pt surface can be characterized reasonably by measurement in the SEM. A typical SEM micrograph used to characterize tip dimensions has been included for a single electrode in Fig. 4b. The tip shown has a 70 ± 10 nm radius, determined by SEM. A cyclic voltammogram (CV) for the oxidation of 1 mM $FcTMA^+$ (0.1 M KCl) at a scan rate of 200 mV s^{-1} is shown in Fig. 5a, which shows a characteristic steady-state response. By holding the tip in bulk solution at the steady-state limiting potential, 0.45 V, a steady current of 2.51 pA was recorded. A non-recessed electrode would have given a steady-state limiting current of 16.2 pA for this electrochemical reaction. If one naively assumed a planar disk geometry, as has sometimes been done in the past, the tip radius would be calculated as 10 nm, using the steady-state limiting current, i_{ss}, equation for a disk electrode (for an infinite RG [41]):

$$i_{ss} = 4nFDc^{*}a \,, \tag{2}$$

where n is the number of electrons transferred and F is Faraday's constant (96 485 C mol^{-1}). That nanoscale tips are often recessed is increasingly recognized and additional characterization methods proposed to determine the geometry have been proposed [42-44]. As highlighted herein, a recessed electrode is actually beneficial for application in IC-SECM as it serves to protect the active part of the tip.

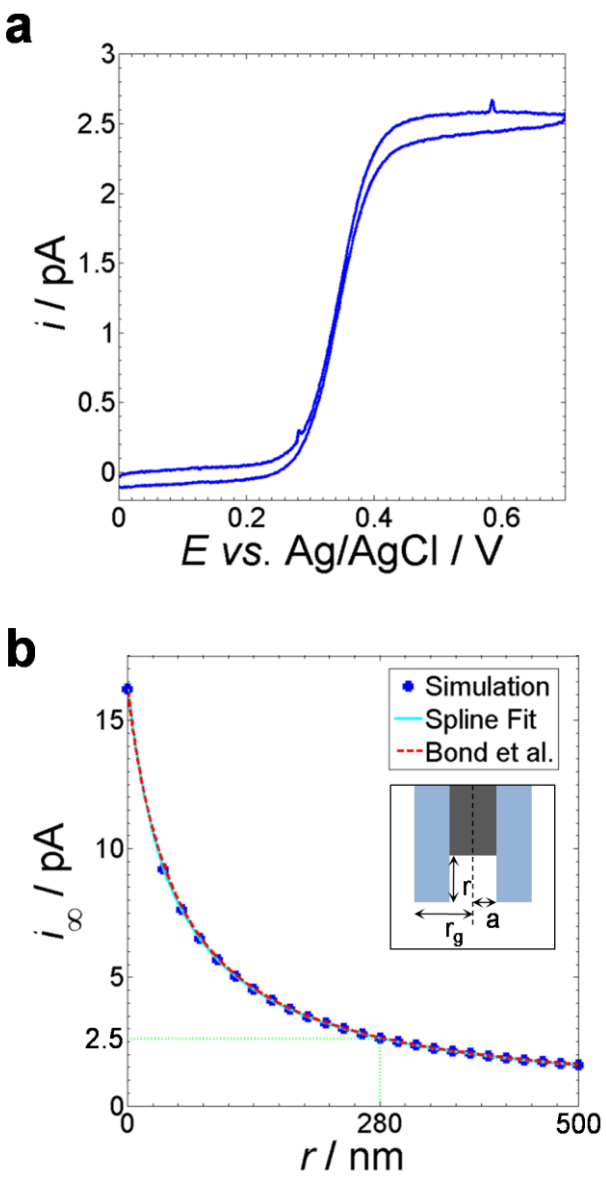

Fig. 5 (a) CV recorded for a 70 nm radius electrode (characterized by SEM) in 1 mM $FcTMA^+$ and 0.1 M KCl, at a scan rate of 200 mV s^{-1}. (b) Simulated steady-state diffusion-limited currents in bulk solution *vs*. Pt recession distance, *r*, in nm for a 70 nm radius planar disk electrode. Simulated results (blue) have been spline fitted (light blue) and theoretical results by Bond *et al.* are shown (red dashed) [45]. The experimental diffusion-limited current, 2.51 pA, (green dotted) was used to determine *r*, for this electrode. Inset shows key tip dimensions: electrode radius, *a*, glass sheath radius, r_g, and Pt recession depth, *r*

The steady-state limiting current for the electrodes were always less than predicted for a non-recessed disk electrode based on SEM measurements of the electrode radius, indicating that the tips were recessed to varying degrees [44-46]. In the case of the tip considered above, the Pt radius as measured in SEM was *ca*. 7 times greater than the radius calculated from the steady-state limiting current in the bulk. We need to consider that this discrepancy could partly be due to charging effects of the Pt sealed in the insulating glass making it appear larger in the SEM than it actually is. This aspect was considered recently by

Tefashe and Wittstock, who studied micropolished Pt electrodes of sub-micron dimensions [47]. In their study, the nanoelectrode and glass sheath were coated in an ionic liquid to reduce such effects [48], yet a similar disparity was observed to that herein (e.g. the radius measured in SEM was 348 nm, *c.f.* 53 nm calculated from i_{ss}). In our case, the electrodes were grounded to the tip holder in the SEM to reduce charging effects.

We conclude that the main reason for the difference in electrode dimensions from SEM and voltammetry is that the electrode is recessed, probably for reasons recently identified by Amemiya and co-workers [49]. Although we cannot rule out some blockage of the active electrode as well, additional information from approach curves indicates that recession is the main reason for the much diminished bulk current (*vide infra*). The extent of recession was estimated via FEM simulations, as described above, using the well characterized electrode dimensions from the SEM measurements. For the tip shown in Fig. 4d, the model predicted a series of diffusion-limited currents in bulk solution for a series of recession depths, *r*, as shown in Fig. 5b (inset). The relationship of limiting current of the tip in the bulk against Pt recession depth shown in Fig. 5b allowed an estimate of 280 nm for the recession depth.

The effect of recession depth on the steady-state limiting current has been studied by others; Bond's model works for deeply recessed electrodes [45], whilst the model by Bartlett applies also to shallow recessed electrodes [46]. It can be seen that the FEM model herein matches reasonably closely to the result by Bond *et al.*, included in Fig. 5b [45]. AFM has also been used to visualize the surface of nanoelectrodes [42], and white light vertical scanning interferometry can be used to measure the recession of an electrode, although this is limited to electrodes of several to several tens of microns dimension [43]. Our approach to measure the recession is fast and simple, based on the characterization by SEM and the diffusion-limited steady-state current.

Approach curves. Importantly, by deploying IC-SECM with nanoelectrodes, we found that the detection of oscillation amplitude damping is possible for small (nanoscale) tips. An amplitude setpoint of 95 % of that in the bulk was used for approach curves and imaging. A typical negative feedback approach curve to glass is shown in Fig. 6a, with the oscillation amplitude, δ, shown in green. In the approach, damping is first observed when the current has fallen by *ca.* 5 %, *i.e.* just beyond the noise level of *ca.* 2 % of the oscillation amplitude, although further extension of the tip into the surface leads to the oscillation amplitude and tip current decreasing further. These needle-type nanoelectrodes possessed a large degree of flexibility in the shaft of the tip, which was advantageous in allowing the tip to bend slightly, rather than snap, as it was pushed against the substrate. Since the alignment between the tip and substrate was unknown, d / a was arbitrarily set to zero at the point of IC detection.

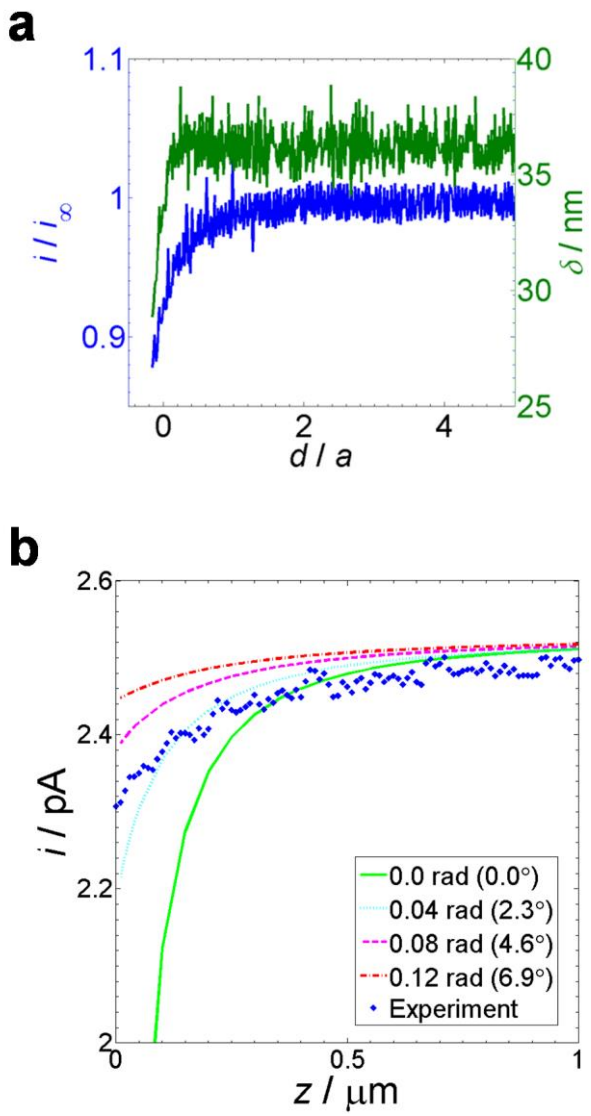

Fig. 6 (a) Feedback approach curve to a glass (insulator) substrate with a 70 nm radius Pt nanoelectrode (characterized by SEM) oscillated at 70 Hz, δ = 36 nm in IC-SECM mode. The electrode potential was fixed at a value where 1 mM $FcTMA^+$ in bulk solution underwent diffusion-limited oxidation at the tip electrode. The normalized current at the tip (blue) and corresponding oscillation amplitude of the tip (green) are shown as a function of the tip-substrate separation where d/a = zero corresponds to IC detection. (b) Simulated approach curves for tip angles with respect to the surface of 0 (green), 0.04 (light blue dotted), 0.08 (pink dashed) and 0.12 radians (red dashed-dotted) against the experimental approach from part (a) (blue)

Using the known recession of the tip from the model shown in Fig. 6b, the same electrode was modeled approaching the surface at different angles in order to find the misalignment between tip and substrate. Here, z = 0 μm corresponds to IC detection (*i.e.* $d \neq 0$ when *alpha* > 0), and the model did not consider tip bending. The low damping setpoint ensures tip bending is minimized. Greater damping could lead to tip bending. IC-SECM detects IC, and there may be tip bending which would occur to a greater extent, the higher the oscillation amplitude damping. To minimize this, we choose the smallest damping factor, that can clearly be discerned (*vide supra*). Since the tip current at the point at which IC was detected did not

drop much beyond 90 % of the bulk current, Fig. 6b shows that the tip was misaligned to the substrate somewhere between 0.04 and 0.08 radians, or about 3 ° or so, which appears reasonable and suggests that recession of the electrode is the main reason for the greatly reduced currents in bulk compared to expectations based on a coplanar electrode of dimensions identified in SEM.

A key component of the soft-tapping IC-SECM setup is the implementation of the piezo bender actuator, in which the tip exerts less force on the sample. Using the manufacturer's spring constants of 0.6 N μm^{-1} for the piezoelectric positioner used in our previous setup (PI Hera P-621.ZCD) and 0.02 N μm^{-1} for the bender actuator implemented in this new setup (PICMA P-871.112) we can estimate the forces applied by the tip on the sample of 3×10^{-3} N and 1×10^{-4} N respectively, based on a displacement of 5 nm from the damping of the oscillation of the tip. These values are upper limits with these nanoscale tips because tip bending may actually greatly reduce the force applied. Thus in this setup, the force of the tip on the sample, when the tip is mounted on the bender actuator is *ca*. 3 % of the force when the tip is mounted directly on to the piezoelectric positioner. The force exerted by the piezo bender actuator is of the same order as found for soft linear array imaging devices [50, 51].

Imaging. A gold band array on glass was used as a substrate for IC-SECM imaging in feedback mode. An optical image of the substrate is given in Fig. 7a. The 125 nm height of the gold band (Fig. 7b) was not detectable in the topography for the area imaged by SECM, since the glass sheath surrounding the Pt nanoelectrode was *ca.* 3.6 μm. The AFM image shows that the edge of the gold band is not perfectly straight due the lift off process in the fabrication of the sample, therefore a rough edge was also expected in the electrochemical image. The radius of the Pt nanoelectrode used for IC-SECM imaging of the sample was 160 nm, as determined by SEM, and a view of the tip above the substrate taken *in-situ* is shown in Fig. 7c.

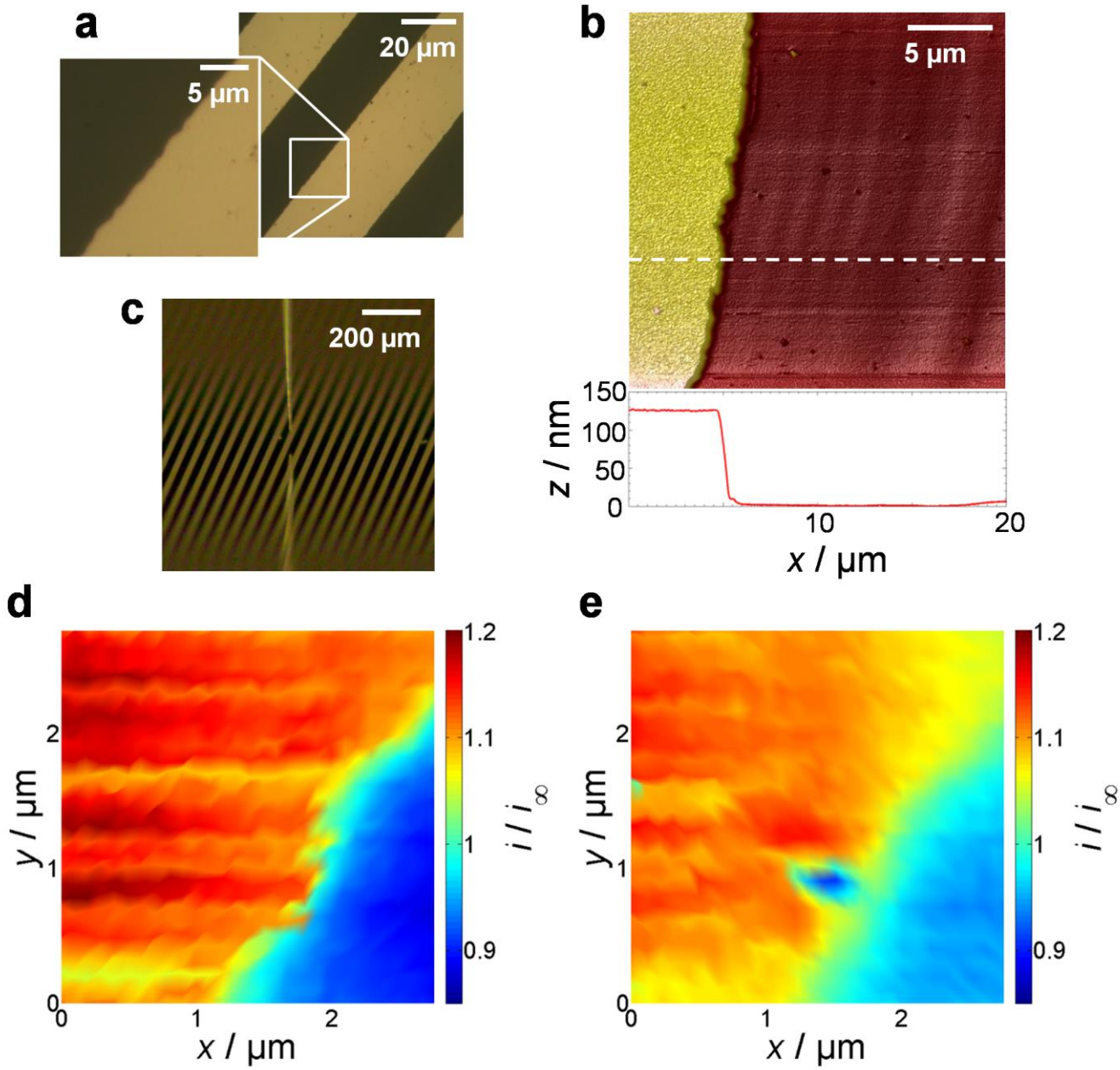

Fig. 7 (a) Optical microscope image of the gold band sample, with a zoomed-in inset over the edge of a gold band. (b) AFM topography image of the substrate with inset of a line scan. (c) View of the tip above the substrate prior to IC-SECM imaging. (d) IC-SECM images of the edge of a gold band on glass, obtained using a 160 nm radius Pt disk electrode (80 Hz, δ = 39 nm, 1 mM $FcTMA^+$). Forward scan in IC of mean tip current/bulk current (d), and reverse scan of mean tip current/bulk current at constant separation of 300 nm (e)

Fig. 7d shows the feedback SECM image recorded with the tip in IC-mode, *i.e.* tracing the contours of the surface. When the tip is over the gold substrate, there is some positive feedback leading to current values with respect to bulk that are enhanced, *i.e.* $i / i_\infty > 1$. Over the glass part of the substrate surface, negative feedback occurs, with diffusion to the tip blocked leading to $i / i_\infty < 1$. For the reverse scan line, the tip was 300 nm away (in the *z*-direction) from the position of IC

with the surface. This image shows both lower resolution and lower deviation of local currents from the bulk current value, since the probe is further away from – and thus less sensitive to the nature of – the surface. The feature exhibiting negative feedback in the reverse scan and positive feedback in the forward scan (at x = 1.5 μm, y = 1 μm) can be attributed to surface contamination during the forward scan of the gold substrate by the tip. This clearly only affects a few pixels on one line in the image, and with the development of hopping IC-SECM [52, 53], we will expect to reduce the amount of contact between the tip and the substrate by > 99 %, which would overcome such problems in the future. Notice that the tip current over the glass (insulator) in Fig. 7e was *ca.* 90 % of that in the bulk, which – although for a different tip – is in line with the approach curve in Fig. 6. The resolution of the tip is clearly much greater than for a typical micron sized UME, since a change from gold to glass occurs over a lateral distance of 200 nm at worst in Fig. 7d.

Conclusions

We have shown that nanoscale imaging is possible with IC-SECM, using Pt-disk electrodes fabricated by laser pulling, and cut to a desired shape by FIB milling. The tips were found to be recessed, and the degree of recession was determined based on the disparity between the steady-state limiting current and the apparent size of the electrode based on SEM measurements. In addition, (mis)alignment between the electrode and the substrate surface was estimated based on the recession depth determined, through approach curve measurements. The recessed nature of these tip electrodes is particularly useful for IC-SECM in that it acts to protect the active electrode when it comes into contact with the surface. Although the results presented herein are for amperometric tips over a model substrate, potentiometric probes could be used with this technique.

The implementation of the piezo-bender actuator was important in the realization of IC-SECM for nanoelectrodes. We anticipate that this technique could be applied to image samples with features of nanometer dimensions, such as individual carbon nanotubes, or low density single-walled carbon nanotube networks. The smaller force of the tip on the sample when using the piezo-bender actuator, as compared to the *z*-piezoelectric positioner used in our previously described setup, could allow for the imaging of softer samples, with greater topographical sensitivity. Future work could also consider the use of hopping scanning [52, 53], to eliminate lateral forces on the tip during the imaging, while allowing the tip to move closer to the sample by increasing the setpoint of the damping of the oscillation amplitude.

Acknowledgements

This work was supported by the Engineering and Physical Sciences Research Council (EPSRC) project studentship for R.L. (Grant EP/H023909/1) and MOAC/DTC studentships for K.M. and M.B. We acknowledge support from a European Research Council Advanced Investigator Grant (ERC-2009-AdG247143 QUANTIF) for P.R.U and K.M. Some of the

equipment used in this research was obtained through Birmingham Science City with support from Advantage West Midlands and the European Regional Development Fund. We thank Robert B. Channon and Andrew J. Soulby for their early contributions to the work. We are grateful to Dr. Alexander W. Colburn for designing and building the electronic instrumentation used herein.

REFERENCES

1. Bard AJ, Fan FRF, Kwak J, Lev O (1989) Anal Chem 61:132-138
2. Amemiya S, Bard AJ, Fan F-RF, Mirkin MV, Unwin PR (2008) Annu Rev Anal Chem 1:95-131
3. Schulte A, Nebel M, Schuhmann W (2010) Annu Rev Anal Chem 3:299-318
4. Kim J, Shen M, Nioradze N, Amemiya S (2012) Anal Chem 84:3489-3492
5. Ludwig M, Kranz C, Schuhmann W, Gaub HE (1995) Rev Sci Instrum 66:2857-2860
6. Cougnon C, Bauer-Espindola K, Fabre DS, Mauzeroll J (2009) Anal Chem 81:3654-3659
7. Ballesteros Katemann B, Schulte A, Schuhmann W (2004) Electroanalysis 16:60-65
8. Etienne M, Anderson EC, Evans SR, Schuhmann W, Fritsch I (2006) Anal Chem 78:7317-7324
9. Lee Y, Ding Z, Bard AJ (2002) Anal Chem 74:3634-3643
10. Buchler M, Kelley SC, Smyrl WH (2000) Electrochem Solid-State Lett 3:35-38
11. Wipf DO, Bard AJ (1992) Anal Chem 64:1362-1367
12. Edwards MA, Whitworth AL, Unwin PR (2011) Anal Chem 83:1977-1984
13. Wipf DO, Bard AJ, Tallman DE (1993) Anal Chem 65:1373-1377
14. Kurulugama RT, Wipf DO, Takacs SA, Pongmayteegul S, Garris PA, Baur JE (2005) Anal Chem 77:1111-1117
15. Takahashi Y, Shevchuk AI, Novak P, Babakinejad B, Macpherson J, Unwin PR, Shiku H, Gorelik J, Klenerman D, Korchev YE, Matsue T (2012) Proc Natl Acad Sci U S A 109:11540-11545
16. Macpherson JV, Unwin PR (2000) Anal Chem 72:276-285
17. Kranz C, Friedbacher G, Mizaikoff B, Lugstein A, Smoliner J, Bertagnolli E (2001) Anal Chem 73:2491-2500
18. Salomo M, Pust SE, Wittstock G, Oesterschulze E (2010) Microelectron Eng 87:1537-1539
19. Kueng A, Kranz C, Mizaikoff B, Lugstein A, Bertagnolli E (2003) Appl Phys Lett 82:1592-1594
20. Dobson PS, Weaver JMR, Holder MN, Unwin PR, Macpherson JV (2005) Anal Chem 77:424-434

21. Burt DP, Wilson NR, Weaver JMR, Dobson PS, Macpherson JV (2005) Nano Lett 5:639-643

22. Fan F-RF, Bard AJ (1999) Proc Natl Acad Sci U S A 96:14222-14227

23. Hansma PK, Drake B, Marti O, Gould SA, Prater CB (1989) Science 243:641-643

24. Takahashi Y, Shevchuk AI, Novak P, Murakami Y, Shiku H, Korchev YE, Matsue T (2010) J Am Chem Soc 132:10118-10126

25. Takahashi Y, Shevchuk AI, Novak P, Zhang Y, Ebejer N, Macpherson JV, Unwin PR, Pollard AJ, Roy D, Clifford CA, Shiku H, Matsue T, Klenerman D, Korchev YE (2011) Angew Chem, Int Ed 50:9638-9642

26. Comstock DJ, Elam JW, Pellin MJ, Hersam MC (2010) Anal Chem 82:1270-1276

27. McKelvey K, Edwards MA, Unwin PR (2010) Anal Chem 82:6334-6337

28. Patten HV, Meadows KE, Hutton LA, Iacobini JG, Battistel D, McKelvey K, Colburn AW, Newton ME, Macpherson JV, Unwin PR (2012) Angew Chem, Int Ed 51:7002-7006

29. McGeouch C-A, Peruffo M, Edwards MA, Bindley LA, Lazenby RA, Mbogoro MM, McKelvey K, Unwin PR (2012) J Phys Chem C 116:14892-14899

30. McKelvey K, Snowden ME, Peruffo M, Unwin PR (2011) Anal Chem 83:6447-6454

31. Mezour MA, Morin M, Mauzeroll J (2011) Anal Chem 83:2378-2382

32. Ballesteros Katemann B, Schuhmann W (2002) Electroanalysis 14:22-28

33. Zuliani C, Walsh DA, Keyes TE, Forster RJ (2010) Anal Chem 82:7135-7140

34. Li Y, Bergman D, Zhang B (2009) Anal Chem 81:5496-5502

35. Cox JT, Zhang B (2012) Annu Rev Anal Chem 5:253-272

36. Laforge FO, Velmurugan J, Wang Y, Mirkin MV (2009) Anal Chem 81:3143-3150

37. Sun P, Laforge FO, Abeyweera TP, Rotenberg SA, Carpino J, Mirkin MV (2008) Proc Natl Acad Sci U S A 105:443-448

38. Shao Y, Mirkin MV, Fish G, Kokotov S, Palanker D, Lewis A (1997) Anal Chem 69:1627-1634

39. Bertoncello P, Ciani I, Li F, Unwin PR (2006) Langmuir 22:10380-10388

40. Cornut R, Bhasin A, Lhenry S, Etienne M, Lefrou C (2011) Anal Chem 83:9669-9675

41. Lefrou C, Cornut R (2010) ChemPhysChem 11:547-556

42. Nogala W, Velmurugan J, Mirkin MV (2012) Anal Chem 84:5192-5197

43. Chang J, Leonard KC, Cho SK, Bard AJ (2012) Anal Chem 84:5159-5163

44. Sun P, Mirkin MV (2007) Anal Chem 79:5809-5816

45. Bond AM, Luscombe D, Oldham KB, Zoski CG (1988) Journal of Electroanalytical Chemistry and Interfacial Electrochemistry 249:1-14

46. Bartlett PN, Taylor SL (1998) J Electroanal Chem 453:49-60

47. Tefashe UM, Wittstock G (2013) C R Chim 16:7-14

48. Arimoto S, Kageyama H, Torimoto T, Kuwabata S (2008) Electrochem Commun 10:1901-1904

49. Nioradze N, Chen R, Kim J, Shen M, Santhosh P, Amemiya S (2013) Anal Chem

50. Cortés-Salazar F, Momotenko D, Lesch A, Wittstock G, Girault HH (2010) Anal Chem 82:10037-10044

51. Lesch A, Momotenko D, Cortés-Salazar F, Wirth I, Tefashe UM, Meiners F, Vaske B, Girault HH, Wittstock G (2012) J Electroanal Chem 666:52-61

52. Lazenby RA, McKelvey K, Unwin PR (2013) Anal Chem 85:2937-2944

53. Novak P, Li C, Shevchuk AI, Stepanyan R, Caldwell M, Hughes S, Smart TG, Gorelik J, Ostanin VP, Lab MJ, Moss GWJ, Frolenkov GI, Klenerman D, Korchev YE (2009) Nat Methods 6:279-281